An ångström-sized window on the origin of water in the inner solar system: Atomistic simulation of adsorption of water on olivine

M. Stimpfl[a],*, A.M. Walker[b,c], M.J. Drake[a], N.H. de Leeuw[d], P. Deymier[e]

[a]*Lunar and Planetary Laboratory, University of Arizona, Tucson, AZ 85721, USA*
[b]*Research School of Earth Sciences, The Australian National University, Mills Road, Canberra, ACT 0200, Australia*
[c]*Department of Earth Sciences, University of Cambridge, Downing Street, Cambridge CB2 1TS, UK*
[d]*Department of Chemistry, University College London, 20 Gordon Street, London WC 1H 0AJ, UK*
[e]*Department of Material Science and Engineering, University of Arizona, Tucson, AZ 85721, USA*

Available online 9 August 2006

Abstract

The origin of water in the inner solar system is not yet well understood. Because of the coexistence of water and small solid particulates in the accretion disk from which our planetary system formed, we propose that adsorption of water onto the surfaces/pores of forsterite could play and important role in the delivery of water to the rocky planets. In this work we employ energy minimization techniques to understand the surface energy structure and the distribution of surface adsorption sites for the $\{0\,1\,0\}$ and $\{1\,0\,0\}$ planes in forsterite. This study indicates that most of the surface area is not involved in the initial adsorption of water molecules and that the stronger adsorption sites coincide with the most underbonded surface Mg atoms.
© 2006 Elsevier B.V. All rights reserved.

1. Introduction

Water is omnipresent on Earth and it is critical to our understanding of the crystal nucleation and growth environment of sedimentary materials. As a result, the water/mineral interface has been investigated by both experimental and computational approaches in order to gain a better insight at the atomic level of the interaction of water with the solid surface (for a recent review, see [1]). A range of state-of-the-art experimental techniques has been applied to investigate the solid/water interface elucidating, for example, the structure of water monolayers at the surface [2,3] and the chemical behavior of water at surface sites [4,5]. This experimental research has been complemented by a series of computational investigations of the water sorption processes occurring at surface sites of different minerals, ranging from simple oxides such as MgO [6,7], TiO$_2$ [8,9] and silica [10–12], to more complex poly-ionic materials, including carbonate [13,14] and phosphate minerals [15,16].

However, the importance of water sorption at the mineral interface is by no means confined to its role in sedimentary processes. It is applicable, for example, to the field of planetary science and, more specifically, to the accretion and growth of planets. Planet formation can be described in three steps [17–20]: (1) dust grains, which condense from or preexist in the accretion disk, aggregate by low energy collisional sticking forming small planetesimals up to 1–10 km in size, (2) at diameters above about 1 km, gravity becomes important and these planetesimals collide and gain mass very quickly by runaway accretion to produce protoplanets with diameters of 1000 km or larger, (3) at any stage in the growth of a planet, the next largest object colliding with a protoplanet is one tenth to one third of the mass of the growing protoplanet, thus leading to very violent, energetic collisions towards the end of planetary growth. These "giant impacts" are energetic enough to melt and differentiate planets into Fe-cores, silicate mantles, crusts, oceans, and atmospheres. It is at this stage that water, if present, would have the most

*Corresponding author. Tel.: +1 520 621 6962; fax: +1 520 626 6647.
E-mail address: mstimpfl@lpl.arizona.edu (M. Stimpfl).

dramatic effect on the geochemical evolution of the planet because it depresses the melting point of silicates, facilitating far more melting for a given amount of energy than would be the case for an anhydrous planet. Water is almost certainly necessary for the early formation of granitic continental cores on Earth (see Ref. [21] for a discussion).

While the steps that describe planet formation are widely accepted, there exists no consensus on the origin of water on Earth or elsewhere in the inner solar system. The theories proposed to explain the presence of liquid water in the inner solar system can be differentiated on the basis of the timing of water delivery with respect to the stages of planet formation, and on the basis of the distance from the sun (the heliocentric distance) at which the hydrous material formed. Water is referred as "endogenous water" if the hydrous material formed at the same heliocentric location as the planet. If hydrous material formed at a different heliocentric location from the planet, it is referred to as "exogenous water". Three scenarios have been proposed.

(a) *The dry-exogenous scenario*: The Earth accreted from anhydrous material and acquired water after more than 85% of its mass was accreted (late in stage 3). Hydrous material, possibly in the form of comets or wet asteroids from heliocentric distances greater than 2.5 AU (where AU stands for Astronomical Unit, the mean distance from the Earth to the Sun) migrated inward and collided with an almost formed planet to deliver volatiles and, perhaps, organic material ([22,23] and references therein).

(b) *The wet-exogenous scenario*: The Earth accreted a mixture of dry and wet material during stages 2–3. This wet material is represented by phyllosilicates that formed in the asteroid belt (42.5 AU), migrated inward due to radial drift and accreted to the growing planetesimal [24].

(c) *The wet-endogenous scenario*: The Earth accreted dry and wet material, with hydrous materials forming in the vicinity of 1 AU.

Geochemistry may be used to investigate these scenarios. The chemical fingerprints of the exogenous sources (comets, asteroids) indicate that the majority of Earth's water could not have been delivered by comets and/or asteroids. In particular, the D/H ratio measured for three comets (Hale-Bopp, Hyakutake, and Halley) is about twice that of terrestrial oceanic water, constraining the contribution of this source to the Earth's water budget to no more than 15% [25]. Other geochemical markers, such as the Ar/H_2O ratio, point to an even more limited contribution of water from comets to the Earth's budget [25,26]. Asteroids are dynamically plausible sources of hydrous material accreting to Earth late in Earth's growth [22]. However, Os isotopes in Earth's mantle rule out known meteorite types as the source of Earth's water [25]. Therefore, we must assume either that the asteroids that brought water to the

Earth had a unique chemical composition or that this source is not responsible for delivering the majority of Earth's water budget.

In the wet-endogenous scenario, hydrous material was incorporated directly into the accreting Earth from the initial stages of its formation, possibly during late stage 1. However, because the P–T conditions in the early accretion disk are not known and are based on models, the existence of hydrous materials in the terrestrial planet region in the early stages of planet formation is linked to the physical conditions postulated for the accretion disk. For example, for an optically thin accretion disk [27] the temperature would be too hot for water to survive as ice, or for hydrous minerals to be thermodynamically stable. However in an optically thick accretion disk [28] temperatures at 1 AU would be cold enough for phyllosilicates to be stable. Currently, hot accretion disk models seem to enjoy a wider support than the cold ones.

In view of these problems with both exogenous and endogenous models for the origin of water in the terrestrial planets, we investigate a new hypothesis. We propose that water incorporation occurred by means of gas-solid interactions, i.e. adsorption, started at stage 1 of planet formation when dust and water gas were still present in the accretion disk.

Dust and water gas were both present in the accretion disk for about 16 million years [29]. Equilibrium calculations show that the H_2O/H_2 ratio in the accretion disk was about 5×10^{-4}, and that it was constant throughout the inner solar system [30], corresponding to $pH_2O \sim 10^{-8}$ bars. Note that the equilibrium partial pressure is probably a lower limit [23,31,32]. Astronomical observations show that dust clouds consist of Mg-rich olivine (Mg_2SiO_4, forsterite), pyroxenes and other refractory minerals with radii $< 1 \mu m$ [33]. Several authors [19,34,35] suggest that these refractory minerals should coalesce during stage 1 of planet formation by means of low-velocity impacts that would create low-density, irregularly shaped fractal structures. The concomitant presence of small fractal particulates with high surface area and of water gas in an environment of low-energy impacts raises the overlooked question of the role of adsorption of water into the building blocks of the rocky planets.

A preliminary investigation into the role of adsorption as a potential mechanism to provide endogenous water for the Earth has shown that between 1 and 3 Earth oceans could be adsorbed onto dust that eventually accreted to form our planet [36,37]. This work, however, does not take into account surface energy, effect of orientation of the surface with respect to the crystal structure, fractal nature of the grain, presence of pores, dislocations, other defects that might facilitate the sequestering of water from the bare surface and the possible formation of covalent bonding due to chemisorption. Covalent bonding is important in that it would maximize the retention of water during stage 2 of planet formation. For stage 3 of planet formation, the gravitational field of the planet should be large enough to

ensure the retention of most of the volatiles, even during high-energy impacts [38].

Encouraged by the positive result obtained by our previous simulations, we propose to refine the model of Stimpfl et al. [36,37] by employing energy minimization (this work) and molecular dynamic techniques (in progress).

Here we focus on the adsorption of water onto forsterite grains, the most abundant mineral observed astronomically [33]. Previous studies of water adsorption at forsterite surfaces have only considered the adsorption of a full monolayer of water, hence providing an average adsorption energy per water molecule [39]. In this work, we are interested in probing the reactivity of the individual surface sorption sites and, to this end, we have used a single water molecule to interact separately with each surface site. Although dissociated water adsorption was calculated to occur at the unstable, and hence more reactive, {110} surface of forsterite [39], only molecular adsorption was calculated to take place at the {100} and {010} surfaces without further dissociation of the adsorbed water [39]. Molecular adsorption was confirmed for the {010} surface by ab initio calculations, where it was even found that initially dissociated water molecules recombined at the surface to form a physisorbed water molecule [40]. As we wish to compare directly the reactivity of the different forsterite surfaces towards water, we have only considered associatively adsorbed water molecules in this work, as in any case the initial step towards dissociative adsorption is via molecular physisorption, which is only followed by dissociation of the adsorbed water molecule when this is thermodynamically feasible.

2. Models and methods

Atomistic simulations require a description of the interatomic forces acting between all atoms in an assembly. We describe these interatomic forces by means of empirically fitted interatomic potentials which decompose the interactions in ionic solids into two groups: long-range electrostatic and short-range potentials [41]. The long-range Coulombic interactions, which are the dominant mode of interaction in ionic materials, are calculated using the Ewald summation method [42,43] to ensure convergence. The short-range interactions are described by means of parameterized analytical potentials, such as the Buckingham potential. Buckingham potentials consist of an exponentially decaying repulsive and an attractive dispersion term which describe, respectively, the short-range repulsion term and van der Waals attractions between neighboring electron clouds.

However, the short-range potentials do not take into account effects due to polarization of ions such as oxygen. This effect is therefore accounted for by the introduction of additional potential parameters in the calculation of the interatomic forces, originating from the shell model of Dick and Overhauser [44], where the charge of the ion is divided into a negatively charged massless shell and a massive positively charged core. The shell and the core are connected by a spring and interact by a harmonic potential, where the polarizability of the ion is described by the spring constant and the charges of the core and shell. Finally, to account for partially covalent bonds, such as in the silica group and in the water molecule, angle-dependent forces are introduced. The potential parameters for the Mg_2SiO_4 material are a combination of the SiO_2 potential of Sanders et al. [45] and the MgO potential of Lewis and Catlow [46]. This combined potential has been used to good effect to model bulk properties of point, line, and planar defects in forsterite [6,39,47–51]. The potential model for the water molecule was derived by Leeuw and Parker [52] and the parameters for its interactions with the substituent ions in the forsterite minerals are taken from hydration studies of MgO [10] and quartz, where the water adsorption energies showed good agreement with experiment [53]. The complete forsterite/water potential model has been used previously to study the interaction of complete monolayers of water with forsterite surfaces, where the agreement between experimental and calculated crystal morphologies showed that the potential model was sufficiently accurate to reproduce the relative surface stabilities [39]. We therefore consider it an appropriate potential model for the work presented in this paper. The complete set of parameters for the potential models used in this work and their analytical expressions are listed in Tables 1a and b.

2.1. Surface simulations

The computational study of surface properties is a two-step process. First, the surfaces must be created from the geometry-optimized bulk material before the surface structure and properties can be optimized and investigated. To create the surface, one needs to specify both the Miller indices of the desired surface {hkl}, which define the orientation of the plane with respect to the bulk material, and also the shift which represents the displacement of the plane relative to the original unit cell. A surface may be built up of many different terminations, each with the same orientation and hence Miller index, all of which need to be taken into account [54]. Finally, one needs to consider the particular type of surface under investigation [55]. According to Tasker [56] an ionic crystal can have three different types of surfaces. Type I consists of stoichiometric charge-neutral sheets parallel to the surface and thus any shift perpendicular to the surface will create planes without dipole moment normal to the surface. Type II is a combination of layers of cations and anions, where the repeat unit of the perpendicular shift again has no dipole normal to the surface. Finally, Type III surfaces always have a dipole perpendicular to the surface regardless of the cleavage shift, which needs to be removed by surface reconstruction or other means before geometry optimization and calculation of any surface properties. Bertaut [57] has shown that the surface energy of a dipolar

Table 1(a)
Potential parameters used in this study

Charges (e)			Core-shell interaction (eV Å^{-2})
Ions	Core	Shell	
Mg	2.00000		
Si	4.00000		
H	0.40000		
Oxide oxygen (O_{OX})	0.84819	−2.84819	74.92
Water oxygen (O_{H_2O})	1.25000	−2.05000	209.45

Buckingham potential	A (eV)	ρ (Å)	C (eV Å^6)
Mg–O_{OX}	1428.5	0.29453	0
Mg–O_{H_2O}	490.0	0.29453	0
Si–O_{OX}	1283.9	0.32052	10.66
Si–O_{H_2O}	562.0	0.32052	10.66
O_{OX}–O_{OX}	22764.3	0.14900	27.88
O_{OX}–O_{H_2O}	22764.3	0.14900	28.92
H–O_{OX}	396.3	0.25000	0
H–O_{H_2O}	396.3	0.25000	10.0

Lennard–Jones potential		A (eV Å^{12})	B (eV Å^6)
O_{H_2O}–O_{H_2O}		39 344.98	42.15

Morse potential	D (eV)	a (Å^{-1})	r_0 (Å)
H–O_{H_2O}	6.20371	2.22003	0.92376

Three-body potential		k (eV rad^{-2})	Θ_0
H–O_{H_2O}–H		4.2	108.69
O_{OX}–Si–O_{OX}		2.1	109.47

Coulombic subtraction		(%)	
H–O_{H_2O}(shell)		50	
H–H		50	

Note: All the two body short range potentials cut off distances are at 10 Å and are between oxygen shells when applicable.

Table 1(b)
Equations for interatomic potentials used in this work

Potential name	Formula
Buckingham	$A \exp(-r/\rho) - Cr^{-6}$
Lennard–Jones	$Ar^{-12} - Br^{-6}$
Morse	$D\{[1 - \exp(-a(r - r_0))]^2 - 1\}$
Spring (core-shell)	$1/2 k_1 r^2$
Three body	$1/2 k_2 (\Theta - \Theta_0)^2$

surface is infinite as the energies of dipolar surfaces do not converge with system size, and the calculation of surface properties of unreconstructed dipolar surfaces is therefore meaningless. The creation of a surface for computational investigation is clearly no trivial task, but simulation codes such as the METADISE code [58] and the GDIS code [59] are available.

In the technique implemented in the METADISE computer simulation code [58], periodic boundary condi-

tions are employed only in two directions in the plane of the surface/interface, whereas there is no periodic boundary in the direction perpendicular to the interface. This implementation automatically avoids undesirable interactions between surfaces/interfaces across a vacuum gap between repeating slabs, which is the more usual set up for the simulation of surfaces with three-dimensional periodic boundary conditions. We used the surface cleaving routines embedded within the GDIS visualization routines to generate surface structures that we then placed in the periodic simulation box. The modelled system therefore consists of repeating forsterite slabs and voids. Particular care was taken in choosing both the size of the vacuum gap and the thickness of the forsterite slab to ensure that (a) the separation distance between interfaces of different slabs was sufficiently large to avoid interactions across the vacuum, and (b) that at the center of the slabs the computed bond distances converged to those of the bulk material, thus being unaffected by the interactions and modifications that occur at the surface. According to

Watson et al. [50] the effects of surface relaxation are surface dependent and can propagate into the crystal for a considerable distance.

The bulk crystal was cleaved to obtain the relevant surfaces using the GDIS code [59]. Free surfaces were created by breaking Mg–O bonds, but leaving the SiO_4 group intact (i.e., no Si–O bond is broken). Previous ab initio calculations have shown that Mg_2SiO_4 (forsterite) is a largely ionic material, where the Si–O bonds are partially covalent but the SiO_4 group acts as a poly-anion [40]. It is thus reasonable to treat the SiO_4 group as an ionic entity and only break the purely ionic Mg–O bonds.

After the surfaces were created, we allowed them to relax in order to reach a minimum energy configuration.

2.2. Calculating water adsorption

The structure and properties of bulk forsterite, which is the pure Mg-end member of the olivine solid solution $(Fe,Mg)_2SiO_4$ and crystallizes in the space group P*bnm*, were modeled using the initial coordinates and cell dimensions from the experimental work of Fujino et al. [60]. In this work, we have employed the GULP code which minimizes the lattice energy using the BFGS local optimization algorithm [54,55] to model both bulk forsterite and the interaction between a water molecule and the non-dipolar terminations of the {1 0 0} and {0 1 0} forsterite surfaces. These surfaces were chosen because they contain a range of different surface features and geometries, and exhibit different surface energies, hence permitting the investigation of the effect of surface stability on the reactivity with water.

A measure of the stability of a surface is the value of its surface energy, with a low-positive value indicating a stable surface. The surface energy, γ, is given by

$$\gamma = (E_s - E_b)/A, \tag{1}$$

where E_s is the energy of the slab containing the surface, E_b is the energy of an equal number of similar atoms in the bulk, and A is the area of the surface. To obtain the energy of surface sites with respect to the interaction with a water molecule, the surfaces were divided into a grid of (x, y) coordinates spaced at an interval of 0.25 Å (see Fig. 1). For a given (x, y) pair, a water molecule was positioned above the surface at a fixed height. To provide atomic scale information about surface adsorption sites, two approaches were followed. In the first approach, the potential energy of the system water plus forsterite was computed by allowing the water molecule to interact with the surface by changing its height (z) and its orientation. In other words, the (x, y) coordinates for the oxygen in the water molecule (O_{H_2O}) were kept fixed. This approach provides a map of the surface potential energy as perceived by a water molecule interacting with a surface. This potential energy $U_{min}(x, y)$ is given by

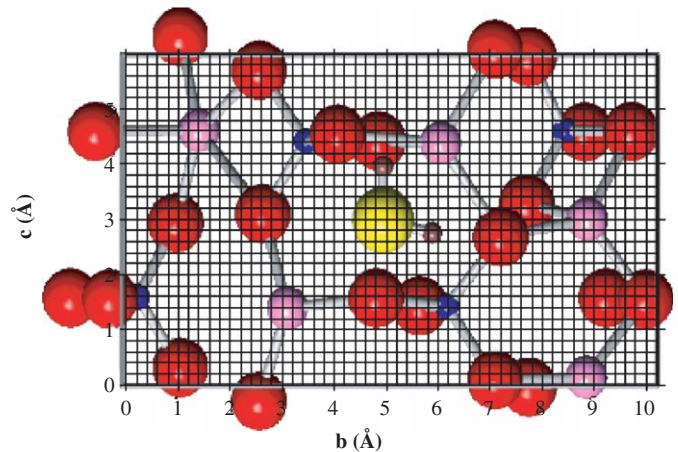$$U_{min}(x, y) = [E_{s+w}(x, y) - (E_s + E_{H_2O})], \tag{2}$$

Fig. 1. Schematic representation of the {1 0 0} surface. Only surface atoms are represented in this figure. Each grid node represents the locus where a water molecule was positioned at the start of the minimization. In this illustration, the water molecule was created at $b = 5$ Å; $c = 3$ Å. Minimization moves the water molecule to the most stable position. In this and all following figures, unless stated differently, from big to small spheres: oxygen, magnesium, silicon and hydrogen atoms. Color scheme: yellow = oxygen in water red = oxygen in lattice; pink = magnesium; blue = silicon; brown = hydrogen.

where $E_{s+w}(x,y)$ is the energy of the slab coordinating the water molecule, E_s is the energy of the dehydrated mineral surface and E_{H_2O} represents the self-energy of the water molecule due to its intramolecular forces $(-877.9 \, kJ \, mol^{-1})$. We have calculated all of the energies with respect to gaseous water, the stable phase for water in the inner accretion disk.

In the second approach, minimizations were carried out by allowing the water molecule to reach a minimum energy configuration with respect to the surface by changing all of its coordinates (x, y, z), if required. This approach gives information both of the preferred adsorption site and its adsorption energy (E_{min}), calculated by

$$E_{min} = [E_{(s+w)} - (E_s + E_{H_2O})]. \tag{3}$$

Negative values for $U_{min}(x, y)$ and E_{min} indicate that the (slab + water) system is more stable than the anhydrous surface. Therefore, the more negative the energy at one grid point, the more stable the (surface + water) complex and the stronger the adsorption site.

3. Results and discussion

3.1. Bulk

The structure of forsterite can be visualized as a distorted hexagonally close-packed array of oxygen with 1/8 of the tetrahedral sites occupied by Si^{4+} and 1/2 of the octahedral sites occupied by divalent cations (mainly Mg^{2+}). Of the two octahedral sites the M1 site, which is more distorted and smaller than M2, forms edge-sharing chains parallel to c (Fig. 2). The tetrahedra are isolated and share oxygen
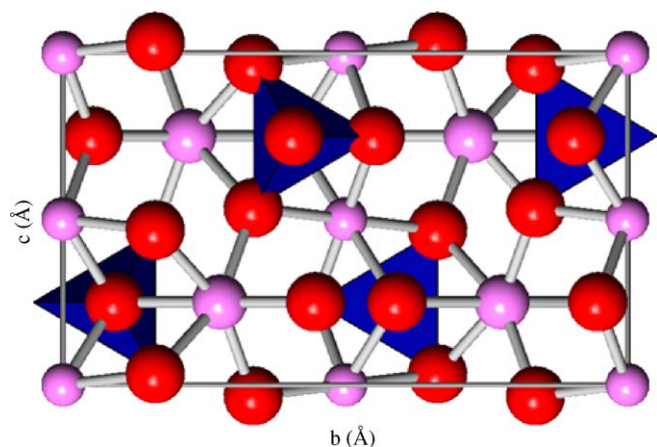
Fig. 2. Bulk forsterite viewed down [1 0 0]. Mg at M2 sites is represented with a slightly bigger sphere than Mg at M1 site. Tetrahedra represent the location of silicon in the structure.

Table 2
Comparison of experimental and calculated values for cell parameters and elastic constants of forsterite

	Calculated	Experimental[a,b]
a (Å)	4.7819	4.7534 (7)
b (Å)	10.2464	10.1902(15)
c (Å)	5.9863	5.9783 (7)
C11	359	329
C22	207	200
C33	281	236
C44	44	67.2
C55	74.5	81.4
C66	84	81.1
C12	94	66
C13	96	68
C23	88	73

[a]Cell data from [60].
[b]Elastic constants in GPa from [61] and references therein.

with adjacent octahedra but not with each other. The average M2-O distance in forsterite is 2.129 Å, while for the M1 octahedron it is 2.093 Å. For the tetrahedra, the average Si–O bond length is 1.634 Å.

In this work, the bulk structure of forsterite compares very well with experimental structures of Iishi [61] as seen in Table 2. The good agreement between the cell parameters and the elastic constants of forsterite for observed and calculated structures validates the choice of the potentials parameters in spite of the fact that they were derived separately for the MgO and SiO$_2$ constituent components of forsterite.

3.2. Pure surfaces

Fig. 3 illustrates the relaxed structures for the two non-dipolar surfaces, {0 1 0} and {1 0 0}, studied in this work. In particular, Figs. 3a and b are a schematic representation of a part of the olivine slab viewed perpendicular to the surface and Figs. 3c and d represent views parallel to the
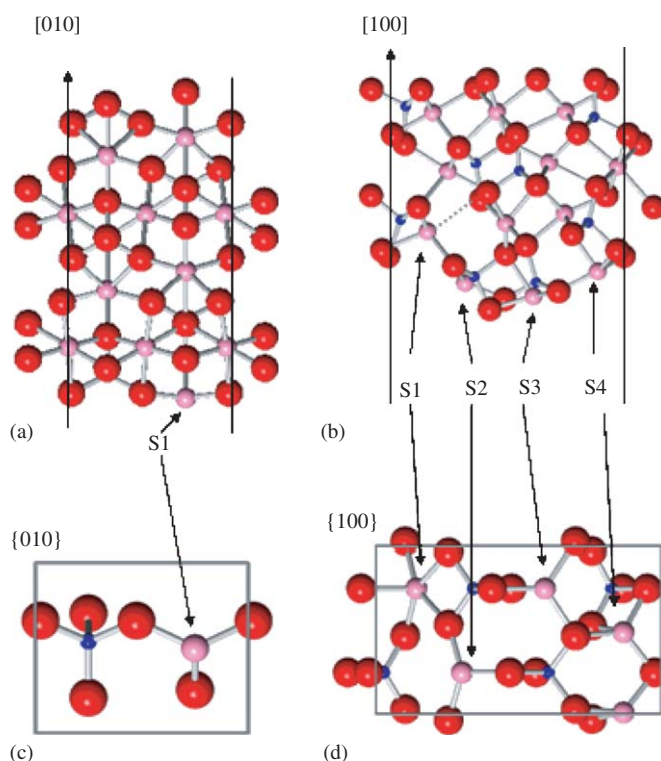

Fig. 3. Schematic representation of part the olivine slabs modeled in this work. In (a) and (b) the planes are viewed perpendicular to the surface. This projection helps identification of the position of the atoms with respect to the free surface. In (c) and (d) the planes are viewed parallel to the surface. This view was created by selecting only the top atomic layer and preserving the oxygen forming the polyhedra. See text for more explanation.

surface unit cell. Table 3 lists the geometric and energetic parameters for both surfaces.

The {0 1 0} surface is a plane with a small surface area of 28.6 Å (Table 3) and it represents one of the major cleavage directions in olivine. The relaxed surface structure of the unit cell is characterized by the presence of one undersaturated Mg ion (S1—Fig. 3) bonded only to three oxygens, two located at surface and one deeper into the inner layers. The Mg–O bond length to the oxygens located at the surface is 1.828 Å, while the third bond, with the oxygen deeper in the structure, is 1.908 Å. These bonds are much shorter than those for the M1-O bonds in bulk olivine and are the result of the un-balanced charge on the surface oxygens and Mg due to the disruption of the octahedron in the formation of the surface. The undersaturated Mg ion sits high on the surface and is surrounded by two rows of oxygens which are lower in the surface, and by a surface tetrahedron. The surface tetrahedron is contracted compared to those in bulk forsterite, with an average Si–O bond distance of 1.630 Å. Other Mg ions visible in Fig. 3a are fully saturated (six Mg–O bonds) and lie deep in the structure. They are thus unavailable as adsorption sites for water or other adsorbates.

The {1 0 0} plane, another cleavage direction in olivine although not so common as {0 1 0}, is a complex plane with

Tables 3

(a) Geometric parameters for the studied surfaces and (b) Unrelaxed and relaxed surface energies for the selected interfaces

Surface	# units	x (Å)	y (Å)	z (Å)	Slab–void (Å)	Surface area (Å^2)
Geometric parameters for the studied surfaces						
{0 1 0}	4	4.7819	5.9863	60	41–19	28.63
{1 0 0}	6	10.2464	5.9863	40	29–11	61.34

Surface	Surface energy[a] (unrelaxed, J/m^2)	Surface energy (relaxed, J/m^2)	Surface energy[b] (relaxed, J/m^2)
Unrelaxed and relaxed surface energies for the selected interfaces[c]			
{0 1 0}	2.23	1.28	1.28
{1 0 0}	8.50	2.57	2.57

units = numbers of forsterite unit cells repeated in the z direction used to create the slab.

[a]This work and [39].

[b][39].

[c]See text for more explanation.

a much larger surface area per unit cell of 61.34 Å (Table 3). As seen in Fig. 3, the relaxed surface structure of the unit cell for {1 0 0} is characterized by the presence of four Mg ions, referred to as S1, S2, S3 and S4. S1 is nested within the surface layer at a depth of roughly 1.4 Å below the plane defined by the oxygens at the surface to which it is bound. S1 is bonded to five oxygens with an average Mg–O bond length of 2.152 Å; of the five anions, three of them are located on the surface and two are located in a deeper layer. In the unrelaxed structure S1 is bonded to six oxygens. After relaxation, however, the sixth bond (dotted line in Fig. 3) appears greatly stretched and is possibly broken as indicated by the long bond length of 2.708 Å (well beyond the Mg–O bond lengths in the bulk material). In spite of the under-bonded nature of S1, its location on the surface seems to prevent water molecules from interacting fully with this Mg ion, as will become clear in the next section. The Mg ion at S2 on the other hand is in an ideal position for water adsorption. This Mg ion sits high on the surface and is bonded to three oxygen atoms. Of these, only one is located at a higher point on the surface than Mg, thus leaving the cation more exposed to water. The average Mg–O bond length for this site is 1.905 Å, giving the site a compact structure. S2 is surrounded by three surface tetrahedra, and two Mg ions. Two of the three tetrahedra are located deeper in the structure compared to S2, and the average Mg-Si distance is 3.345 Å, much longer than that in bulk olivine (2.694–3.277 Å). One might expect that the open geometry at the S2 sites will make it a favorable site for adsorption. The Mg ion at the S3 site also sits high on the surface and is bonded to four oxygens, three located at the surface and one deeper in the structure with an average Mg–O bond length of 2.055 Å. This site is nested between two surface tetrahedra. Finally, the Mg at the S4 site is characterized by the presence of four bonds with oxygens, three on the surface and one deeper in the structure as was seen for S3. The S4 site average Mg–O bond length is 1.963 Å, i.e. shorter than for S3.

As shown in Table 3 for both faces there is a large decrease in surface energy after relaxation. In particular the surface energy for {0 1 0} drops from 2.23 to 1.28 J/m^2, making it the most stable surface before and after relaxation. For {1 0 0} the surface energy drops from 8.50 to 2.57 J/m^2 or about 70%. In general, the surface energy reflects the number of surface ions that have under-saturated bonds, i.e. under-bonded atoms. For ionic materials the electrostatic valence bond (*e.v.b.* = ion charge/coordination number) also known as "Pauling bond strength" predicts the maximum number of bonds that each ion needs in order to be charge-balanced. For example, in bulk forsterite each Si–O bond has an *e.v.b.* of 1 (tetrahedra) while each Mg–O bond has an *e.v.b.* of $\frac{1}{3}$ (octahedra). Consequently, oxygens in addition to being involved in the tetrahedra, have enough charge to further bond to three Mg ions in the structure. The creation of free surfaces, which breaks Mg–O bonds, leaves under-bonded ions at the surface and therefore increases the surface energy of the plane.

During relaxation, the decrease in surface energy is accomplished by an extensive reorganization of the atomic layers close to the surface which is achieved by rotation of the tetrahedra, movement of the magnesium ions towards the surface, and a general tightening of the structure in the attempt to reduce the surface area of the face and to reduce the 'charge imbalance' of the surface atoms by shortening of the bond distance. These rearrangements might be so severe as to result in a loss of point symmetry in the surface layer as observed, for example, for calcite [62].

Thus the low surface energy of the {0 1 0} surface both before and after relaxation reflects the breaking of few bonds with a resulting structure similar to the bulk termination in forsterite [39]. The tight bonds of the surface atoms allow for a smoothening of the unrelaxed surface accomplished also by displacement of the magnesium ion (S1) into the surface by about 0.6 Å. Only one under-bonded Mg atom is left on the surface, which results in a surface that is very stable and with only one potentially

available adsorption site, represented by the Mg at S1 (Fig. 3).

On the other hand, the creation of the {1 0 0} surface causes the breaking of many bonds leaving several under-saturated Mg ions at the surface. The relaxed configuration for {1 0 0} is reached by rotation of the tetrahedra and migration of Mg ions towards the surface. For example, S1 has a net movement toward the surface of 0.8 Å and, in an attempt to smooth the surface, one S1–O bond becomes greatly stretched and possibly breaks as well. The process of surface relaxation for {1 0 0} culminates in the formation of a complex stepped surface with at least three potential sites for adsorption (Fig. 3).

Finally, comparison of the surface energies obtained in this work with those computed by de Leeuw et al. [39] using the METADISE code (Table 3), as mentioned above, shows an excellent agreement, indicating that the slabs and vacuum gaps employed in this work are of an appropriate size (Table 2).

3.3. Surface potential energy and adsorption sites

The surface potential energy plots, which represent a projection of $U_{\min}(x, y)$ at the grid point (x, y) for the planes studied in this work, are shown in Figs. 4a and 5a for {0 1 0} and {1 0 0}, respectively. Figs. 4b and 5b display the energy contours for the surface potential energy plots and the preferred site of adsorption for a water molecule, for {0 1 0} and {1 0 0}, respectively. The preferred site of adsorption was identified by energy minimization technique where the water molecule was allowed to vary all of its coordinates (i.e. x, y, z) during the minimization. These last sets of minimization will be referred to as "full minimization scans". In a number of cases the "full minimization scans" failed to find a true minimum on the potential energy surface as revealed by the presence of imaginary phonon frequencies at the gamma point and by an "optimized" structure that identified sites of adsorption, with energies in excess of $-100\,\mathrm{kJ/mol}$, on a surface potential energy maximum. We found that re-optimization using the mode following rational function optimiser [63] avoided this problem and the structure relaxed to a true minimum energy configuration. We chose not show the results of the failed structural optimizations using the BFGS minimization in Figs. 4b and 5b if their energies were greater than $-100\,\mathrm{kJ}$. However, it is worth mentioning that for the {1 0 0} surface, only ~10% of all the minimizations where water was free to move across the surface failed to reach a true minimum. Few anomalous runs for the {0 1 0} surface are present in Fig. 4b because their $E_{\min}$ are smaller than $-100\,\mathrm{kJ}$.

As mentioned previously, energies of interaction between water molecules and surfaces, here referred as $U_{\min}(x, y)$ and $E_{\min}$ as a function of the minimization technique employed, are negative and the more negative the energy, the stronger the interaction or the site is. However, to simplify the text, from here onwards, we will report and discuss these energies in terms of their absolute values so that the reported energy is that required to remove the water molecule from the surface and return it to the gas phase.

In all the simulations, the system "surface plus water" is more stable than the anhydrous surface. For {0 1 0} the average $E_{\min}$ is 106 kJ/mol (± 26) kJ/mol and 134 kJ/mol (± 35) kJ/mol for {1 0 0}. These values are in good agreement with previous calculations of surface adsorptions by de Leeuw et al. [39] and again reflect the relative stabilities of the two faces, with the most unstable one showing a greater affinity for water.

For the {0 1 0} surface, Fig. 4a shows a region on the surface potential map characterized by high values of $U_{\min}(x, y)$ ranging from 135 to 100 kJ/mol and localized around the S1 site (Fig. 3). The energy barrier that separates S1 sites along the **c** direction is ~60 kJ/mole while along the **a** direction is ~20 kJ/mole lower. Thus any surface water diffusion would have a favorable path along the **a** direction. Fig. 4b highlights the presence of five different loci for water adsorption as identified by the "full minimization scans", labeled S1a through S1e. The adsorption energies ($E_{\min}$, Eq. (3)) at S1b and S1d are 103 kJ/mol and at S1a and S1e 128 kJ/mol. While more than 97% of the simulations identify these four sites as the preferred loci for water adsorption on {0 1 0}, a very small fraction of simulations (16 runs) placed the water molecule at the S1c site which has an average adsorption energy of 132 kJ/mol. Even though the S1c locus is the stronger adsorption site, with the highest $E_{\min}$, it fails to attract many water molecules. This non-intuitive result is probably because the water is forced in a different direction before it ever gets to S1c and then falls into another (local) minimum. As seen from Figs. 4a and b the S1c site is in a very specialized position, which seems not readily accessible as the other loci.

Examples of the complex water/surface at selected sites are shown in Figs. 4c and d, where the O_{H_2O} is represented in yellow. Fig. 4c depicts the geometry at the S1c site. The water molecule, which lies parallel to the surface [39] forms two hydrogen bonds with the O_{Ox} at a distance of 1.793 Å, and it coordinates the Mg_{Ox} at a distance of 1.955 Å. The angles $O_{H_2O}-H\cdots O_{Ox}$ and $O_{Ox}\cdots O_{H_2O}-H$ are 151° and 18.1°, respectively, and are close to those for liquid water (162° and 12°, respectively) [64]. This arrangement produces a very stable configuration that results in the high $E_{\min}$ observed at this site. Fig. 4d illustrates the coordination of a water molecule at the S1d site. In this position the water molecule forms two hydrogen bonds, one with O_{Ox} at a distance of 1.644 Å, and another with a bond length of 1.944 Å with Mg_{Ox}. The angles $O_{H_2O}-H-O_{Ox}$ and $O_{Ox}-O_{H_2O}-H$ are very different from those in liquid water. Possible impingement from other surface atoms forces the water molecule to rotate relative to the surface, thus excluding the possibility of coordination of both hydrogens with surface oxygens to reach a more stable configuration.
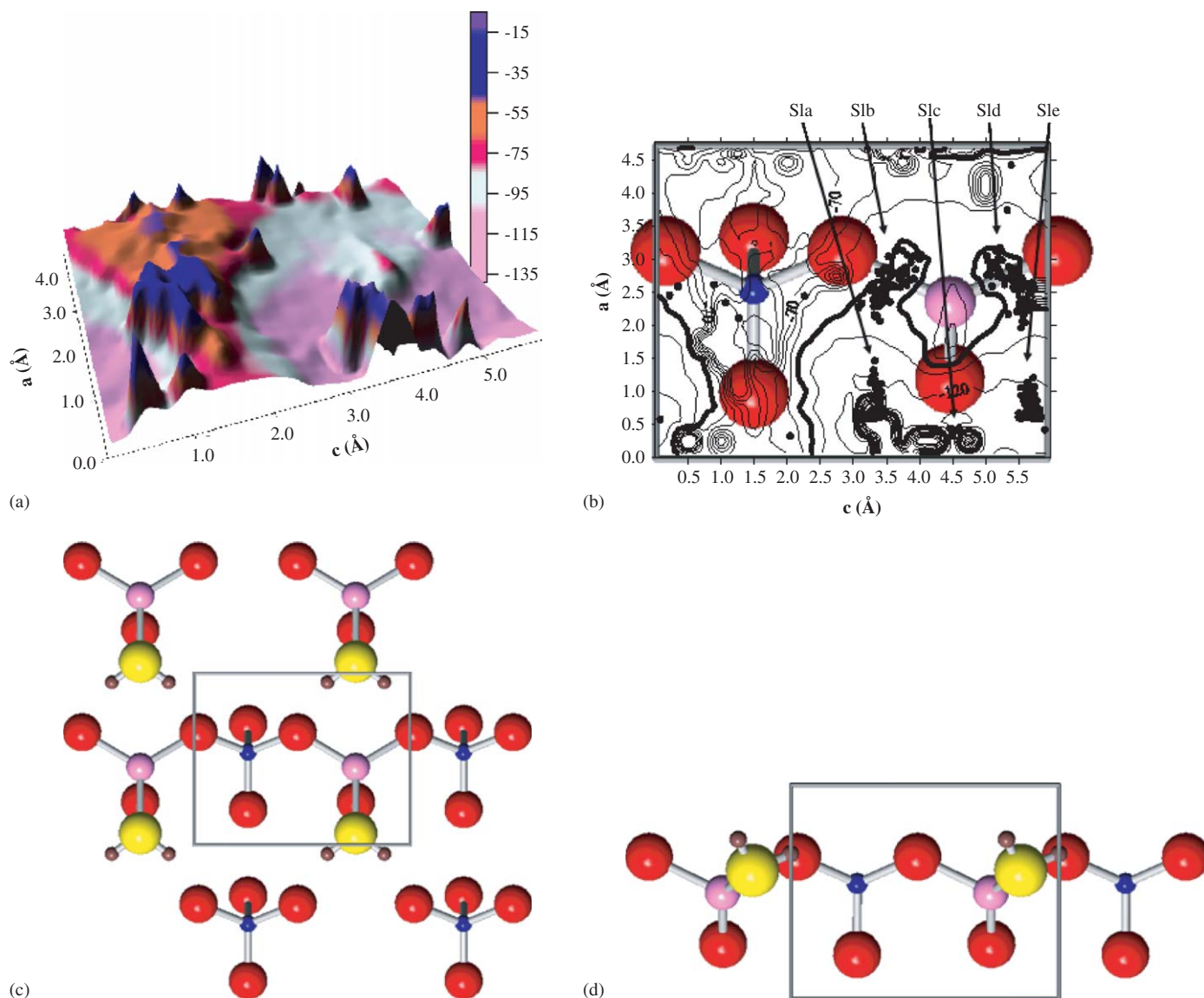
Fig. 4. (a) surface energy potential map for {0 1 0} color scale represents energy in kJ/mole; (b) Surface energy potential contours overlaid on the surface unit cell for the {0 1 0} plane; black dots represents the final resting position for the water molecule whose position was minimized in a series of "full scan minimizations". Thick contour line = 100 kJ/mole level; contour lines at an interval of 10 kJ/mole. (c) Schematic representation of a water molecule in coordination with the surface at the S1c site. (d) Schematic representation of a water molecule in coordination with the surface at the S1d site. Here and in all other figures the O_{H_2O} is the biggest atom (yellow in colored pictures); hydrogen bonds are represented by dotted lines.

For the {1 0 0} surface, Figs. 5a and b show the presence of several adsorption sites, and of potential energy wells localized at the S2, S3 and S4 sites (Fig. 3). As expected the site S1 fails to attract water molecules, in spite of being underbonded, because it lies deeper in the structure and is surrounded by surface oxygens. The S2 site is well defined in the surface energy potential map with a $U_{min}(x, y)$ ranging from 160 kJ/mole at the bottom of the well to 85 kJ/mole at its rim. For the S3 site, the surface potential energy map identifies an adsorption site with a shallower energy structure with respect to S2. Its potential energy varies from 130 to 85 kJ/mole at the rim. Furthermore, while S2 and S3 are separated by an energy barrier of ~75 kJ/mole, S3 and S4 have only a small energy barrier

(~45 kJ/mole) dividing them. The S4 site is the least defined in the surface potential energy map with very shallow and broad minima. Its highest $U_{min}(x, y)$ is ~130 kJ/mole, similar to S3. The energy barrier between different S2 sites is about 85 kJ/mole, whereas between two S3 sites and two S4 sites it is in excess of 100 kJ/mole. Water surface diffusion on this face, if any, seems most favorable along a zigzag path that moves water molecules between S2 and S3 sites, in the general **c** direction.

On close inspection of Fig. 5a, one can identify a very deep trough ($b = 1.0$ Å, $c = 0$–5.98 Å) with a $U_{min}(x, y)$ reaching 230 kJ/mole. However, very few water molecules (less than 10) seem to coordinate to S4 from this region (Fig. 5b). Figs. 5c–f show the geometry for the water
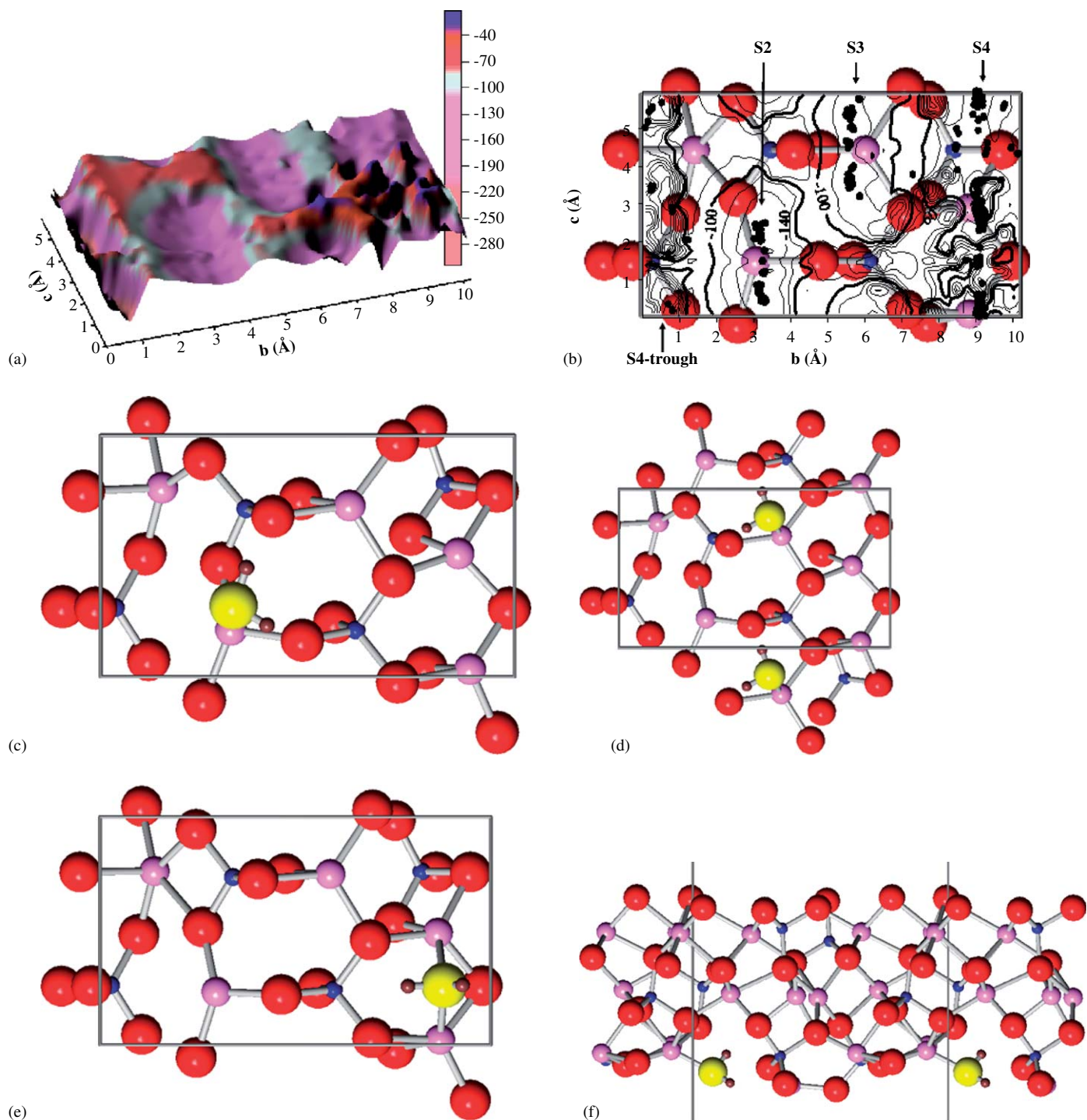
Fig. 5. (a) Surface energy potential map for {1 0 0} color scale represents energy in kJ/mole; (b) surface energy potential contours overlaid on the unit cell for the {1 0 0} plane; black dots represents the final resting position for the water molecule whose position was minimized in a series of "full scan minimizations". Thick contour line = 100 kJ/mole level; contour lines at an interval of 20 kJ/mole (c) schematic representation of a water molecule in coordination with the surface at the S2 site. (d) Schematic representation of a water molecule in coordination with the surface at the S3 site. (e) Schematic representation of a water molecule in coordination with the surface at the S4 site. (f) Schematic representation of a water molecule localized in the potential energy trough.

molecule–surface complex for the three main adsorption sites and for a molecule in the trough. In all cases shown in Fig. 5, except for the configuration shown in Fig. 5e for S4, the Mg–O_{H_2O} distances are less than 2.000 Å and the hydrogens in the water molecules establish two hydrogen

bonds with the O_{Ox} at distances close to 1.8 Å. The coordination of the water molecule located in the trough of potential energy establishes a fourth bond with the surface at the slightly longer distance of 2.03 Å (Fig. 5f). It is worth noting that the water in coordination with S4 in this

position adsorbs in the gap on the surface and creates a surface distortion that has the final effect of smoothing the surface (compare with Fig. 3b). This effect might explain the large adsorption energy at this site.

In all simulations, the water molecule tends to adopt a coordination with the surface consistent with the characters of a hydrogen bond (according to Kamb [65], the distance of an hydrogen bond is of the order of 1.8 Å, while according to Kahn [27] hydrogen bonds are broken if the bond length is greater than 3.1 Å and/or the bond angle (O–H⋯O) is less than 143°). In all the simulations, the number of hydrogen bonds is maximized, with the general trend that the higher the number of bonds, the more stable the water/surface complex and the higher the site energy. The establishment of hydrogen bonds induces some rearrangements to the surface atoms that create slightly different surface structures compared to the relaxed anhydrous surfaces, which explain the distortion in the unit cells shown in Figs. 4c and d and 5c–f compared to the relaxed structures of Fig. 3.

For all the "full minimization scans" that locate the water molecule in energy potential wells, there is at least one bond within the range of a hydrogen bond interaction.

The $Mg-O_{H_2O}$ distance in the interaction between water and olivine is generally less than 2.0 Å, while the O_{Ox}–H ones are close to 1.8 Å. For all the runs, the H coordinates to O_{OX} and the O_{H_2O} bonds to the Mg ions on the surface, as typical for coordinative adsorption [66]. Angles between the water molecule and the surface ions sometimes resemble those observed between water molecules. For example, several runs place the water in coordination with Mg such that the angle $Mg\cdots O_{H_2O}-H$ is close to 109°, which could indicate the involvement of the lone pair of the oxygens in the formation of the bond as seen for water adsorption on pyrite by Stirling et al. [67]. As is the case in liquid water, one can expect the bond strength of the hydrogen bond with forsterite to depend on its length and angle. This fact is reflected, for example, in the different average value for E_{min} at the S1 site on the {0 1 0} surface which stem from the different geometry of the complex "water + surface". Furthermore, the surface potential energy scans for both {0 1 0} and {1 0 0} surfaces (Figs. 4a and 5a) show that, in general, potential energies lower than 80 kJ/mol are localized in the proximity of surface tetrahedra and oxygens, while energy wells of more favorable potential energies coincide with the position of Mg atoms that are accessible on the surface.

For both surfaces studied in this work, most of the surface does not attract any water molecules, thus being "hydrophobic" with respect to the first water molecule to be adsorbed by the surface (see Figs. 4b and 5b). Following Leed and Pantano [68], in Figs. 6a and b we show the distribution of energy for the surface sites for the {0 1 0} and {1 0 0} surfaces, respectively. By comparison with Figs. 4b and 5b, one can conclude that only sites with adsorption energies greater than 100 kJ/mol on the {0 1 0} and 120 kJ/mole on the {1 0 0} surfaces are capable of
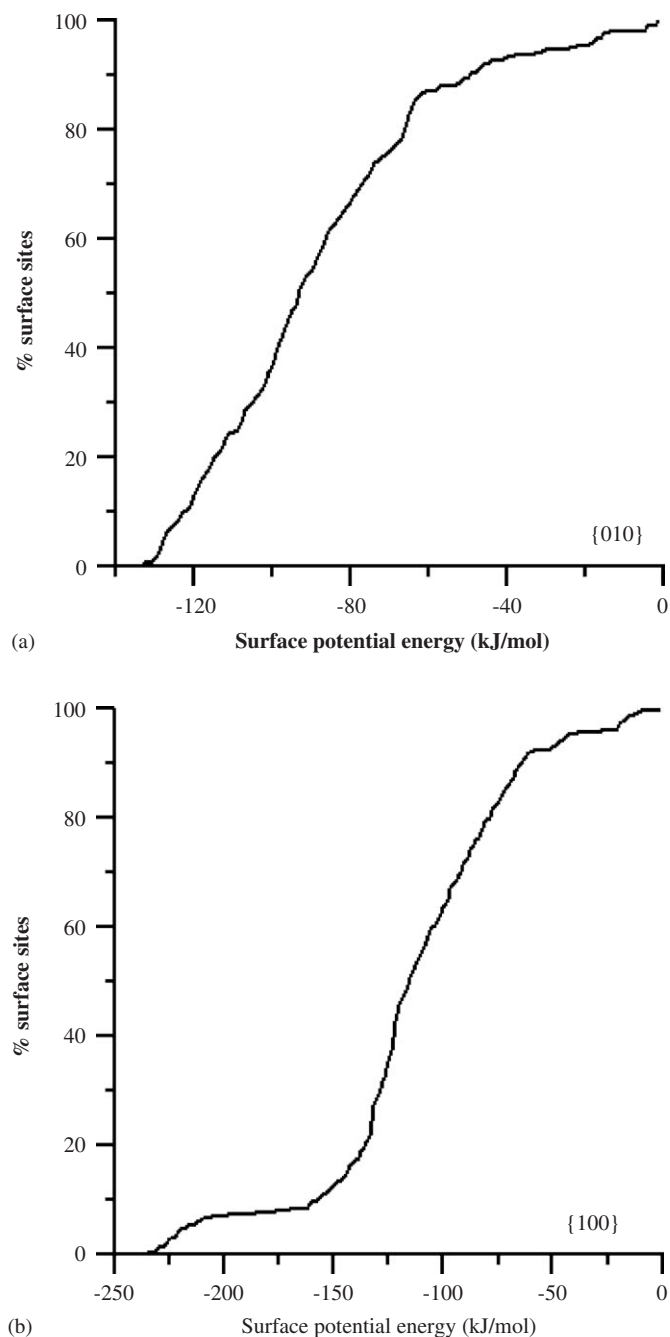

Fig. 6. Energy distribution on olivine surfaces. (a) {0 1 0}; (b) {1 0 0}.

attracting the first water molecules which means that only ∼36% and ∼45% of the surfaces for {0 1 0} and {1 0 0}, respectively, are able to fulfill such requirement.

However, in spite of the greater than 50% "hydrophobic" surface area on these planes, there is the possibility to have multiple water molecules coordinating to the same surface Mg as shown by the presence of several locations where the water molecule can reach a good coordination with the surface (Figs. 4 and 5). Multiple water molecule adsorbed on one surface Mg, were observed on the {0 1 0} plane after we carried out a minimization with four water
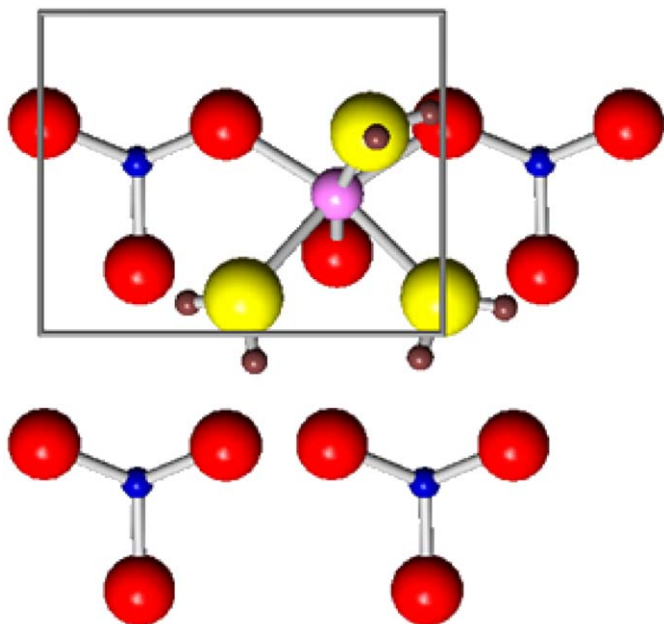
Fig. 7. Schematic representation of the {0 1 0} surface atoms. We have included tetrahedra outside the surface unit cell to exemplify the geometry between the water molecules and the atoms in the crystal lattice. Notice that the Mg atom coordinates three water molecules.

molecules present concomitantly in the unit cell. The initial coordinates for the water molecules were chosen within the S1a-b-d-e clusters and we employed the RFO minimization algorithm for this simulation. Of the four molecules, three maintained their coordination with Mg as shown in Fig. 7. Furthermore, the arrangement of the water molecule around the Mg atoms resembled the geometry of the single molecule at each site (see for example Fig. 4d) and that of bulk oxygens in the octahedra. The creation of clusters of water molecules around surface Mg has also been observed by de Leeuw et al. [39]. We also observe that approximately a water molecule per $10 \, \text{Å}^2$ can be accommodated on the surfaces here studied.

4. Conclusions

As expected by the inspection of the relaxed surface structures, the surface potential energy scans and the "full minimization scan" identify active adsorption sites in correspondence with underbonded surface Mg atoms. The energies of these sites reflect the extent of the undersaturation at the adsorption sites, where the more negative the E_{min} and $U_{min}(x, y)$ the more underbonded the site and the stronger the interaction between water and the surface.

For the {0 1 0} surface only one adsorption site was identified. However, this site shows five possible loci where water molecules can be adsorbed. Interaction energies at this site range from ~100 to 130 kJ/mole. Multiple water molecules coordinating at this site have been observed. For the {1 0 0} surface we identified three the

adsorption sites, characterized by three (S2) or two (S3 and S4) missing bonds, which in order of decreasing strength are S2 (160 kJ/mol) > S3 ~S4 (130 kJ/mol) ≫ S1. Note that for S2 a very specialized adsorption geometry gives rise to a higher adsorption energy and that S1, in spite of being underbonded does not adsorb any water because of its location deeper in the surface. The effect of underbonding on the strength of the adsorption sites was also observed by Leed and Pantano [66] on glass fracture surfaces. The adsorption energies observed in the present work are in excellent agreement with those observed in previous studies [39,67].

For all adsorption sites identified in this work, the water molecule coordinates to the surface by hydrogen-type bonds between $Mg_{Ox} \cdots O_{H_2O}$ and $H \cdots O_{Ox}$, and assumes a geometry that tends to resemble the structure in liquid water, where possible. Future work will continue energy minimization for the {1 1 0} surface of forsterite which is least stable surface for forsterite and exhibits several surface Mg atoms with various degrees of underbonding. We also plan to apply molecular dynamic simulations to the various surfaces to allow temperature to be included in the calculation and might allow modeling of surfaces with a higher degree of non-stoichiometry. The results from these simulations will be used to predict the amount of water that can be adsorbed on silicates in the accretion disk. At this point, it seems possible that Earth's water could be directly adsorbed on to grains in the accretion disk in the earliest stages of planet growth.

Acknowledgments

Reference

[1] M.A. Henderson, Surf. Sci. Rep. 46 (2002) 1.
[2] C.Y. Ruan, V.A. Lobastov, F. Vigliotti, S.Y. Chen, A.H. Zewail, Science 304 (2004) 80.
[3] P. Geissbuhler, P. Fenter, E. DiMasi, G. Srajer, L.B. Sorensen, N.C. Sturchio, Surf. Sci. 573 (2004) 191.
[4] H. Onishi, C. Egawa, T. Aruga, Y. Iwasawa, Surf. Sci. 191 (1987) 479.
[5] S.L.S. Stipp, Mol. Simul. 28 (2002) 497.
[6] W. Walker, J.D. Gale, B. Slater, K. Wright, Phys. Chem. Chem. Phys. 7 (2005) 3235.
[7] W. Langel, M. Parrinello, Phys. Rev. Lett. 73 (1994) 504.
[8] P.J.D. Lindan, N.M. Harrison, M.J. Gillan, Phys. Rev. Lett. 80 (1998) 762.
[9] A. Tilocca, A. Selloni, J. Phys. Chem. B 108 (2004) 4743.
[10] N.H. de Leeuw, G.P. Watson, S.C. Parker, J. Chem. Soc. Faraday Trans. 92 (1996) 2081.
[11] Z. Du, N.H. de Leeuw, Surf. Sci. 554 (2004) 193.
[12] G.M. Rignanese, J.C. Charlier, X. Gonze, Phys. Chem. Chem. Phys. 6 (2004) 1920.

[13] N.H. de Leeuw, S.C. Parker, J. Chem. Soc. Faraday Trans. 93 (1997) 467.
[14] S. Kerisit, S.C. Parker, J. Am. Chem. Soc. 126 (2004) 10152.
[15] D. Mkhonto, N.H de Leeuw, J. Mater. Chem. 12 (2002) 2633.
[16] N.H. de Leeuw, J. Phys. Chem. B 108 (2004) 1809.
[17] G.W. Wetherill, G.R. Stewart, Icarus 106 (1993) 190.
[18] G.W. Wetherill, Geochim. Cosmochim. Acta 58 (1994) 4513.
[19] S.J. Weidenschilling, J.N. Cuzzi, Protostar and Planets, vol. III, University of Arizona Press, Tucson, London, 1999 (p. 1031).
[20] J.E. Chambers, G.W. Wetherill, Icarus 136 (1998) 304.
[21] M.J. Drake, H. Campis, in: Proceedings of the International Astronomical Union, vol. 1, S229 (2006) 381.
[22] A. Morbidelli, J. Chambers, J.I. Lunine, J.M. Petit, F. Robert, B. Valsecchi, K.E. Cyr, Met. Planet. Sci. 35 (2000) 1309.
[23] M.J. Drake, Met. Planet. Sci. 40 (2005) 519.
[24] F. Ciesla, D. Lauretta, Earth Planet. Sci. 231 (2005) 1.
[25] M.J. Drake, K. Righter, Nature 416 (2002) 39.
[26] T.D. Swindle , D.A. Kring, XI Goldschmidt Conference, (2001) LPI Cont. No. 1088.
[27] A. Khan, J. Phys. Chem. 104 (2000) 11268.
[28] E.I. Chiang, B. Goldreich, Astrophys. J. 490 (1997) 368.
[29] J.B. Pollack, O. Hubicky, P. Bodenhaimer, J.L. Lissauer, M. Podolak, Y. Greenzweig, Icarus 124 (1996) 62.
[30] K. Lodders, Astrophys. J. 591 (2003) 1220.
[31] R.N. Clayton, Oxygen in the Terrestrial Planets, (2004) LPI Cont. no. 1203.
[32] J.N. Cuzzi, M. Petaev, E.R.D. Scott, S.J. Weidenschilling, F.J. Ciesla, Chondrites and Protoplanetary Disks. (2004) LPI Cont. 1218.
[33] R.v. Boekel, M. Min, Ch. Leinert, L.B.F.M. Waters, A. Richichi, O. Chesneau, C. Dominik, W. Jaffe, A. Dutrey, U. Graser, Th. Henning, J. de Jong, R. Köhler, A. de Koter, B. Lopez, F. Malbet, S. Morel, F. Paresce, G. Perrin, Th. Preibisch, F. Przygodda, M. Schöller, M. Wittkowski, Nature 432 (2004) 479.
[34] J. Blum, G. Wurm, Icarus 143 (2000) 138.
[35] M. Fogel, C.M. Leung, Astrophys. J. 501 (1998) 175.
[36] M. Stimpfl, M.J. Drake, D.S. Lauretta, Am. Geophys. Soc. 2004.
[37] M. Stimpfl, D.S. Lauretta, M.J. Drake, MAPS 39 (2004) Abstract no. 5218.
[38] H. Genda, Y. Abe, Icarus 164 (2003) 149.
[39] N.H. de Leeuw, S.C. Parker, C.R.A. Catlow, G.D. Price, Phys. Chem. Min. 27 (2000) 332.
[40] N.H. de Leeuw, J. Phys. Chem. B 105 (2001) 9747.
[41] M. Born, K. Huang, Am. Mineral., Dynamical theory of crystal lattices, Oxford University Press, Oxford, 1954.
[42] P.P. Ewald, Ann. Phys. 64 (1921) 253.
[43] M.P. Tosi, Sol. State. Phys. 16 (1964) 1.
[44] B.G. Dick, A.W. Overhauser, Phys. Rev. 112 (1958) 90.
[45] M.J. Sanders, M. Leslie, C.R.A. Catlow, J. Chem. Soc. Chem. Commun. (1984) 1271.
[46] G.V. Lewis, C.R.A. Catlow, J. Phys. C: Solid State Phys. 18 (1985) 1149.
[47] G.D. Price, S.C. Parker, M. Leslie, Mineral. Mag. 51 (1987) 157.
[48] S.C. Parker, G.D. Price, Adv. Solid St. Chem. 1 (1989) 295.
[49] K. Wright, C.R.A. Catlow, Phys. Chem. Min. 20 (1994) 515.
[50] G.W. Watson, P.M. Oliver, S.C. Parker, Phys. Chem. Min. 25 (1997) 70.
[51] A.M. Walker, K. Wright, B. Slater, Phys. Chem. Min. 30 (2003) 536.
[52] N.H. Leeuw, S.C. Parker, Phys. Rev. B 58 (1998) 13901.
[53] N.H. de Leeuw, F.M. Higgins, S.C. Parker, J. Phys. Chem. B 103 (1999) 1270.
[54] J.D. Gale, J. Chem. Soc. Faraday Trans. 93 (1997) 629.
[55] J.D. Gale, A.L. Rohl, Mol. Sim. 29 (2003) 219.
[56] P.D. Tasker, J. Phys. Chem. 12 (1979) 4977.
[57] F. Bertaut, Comptes Rendu 246 (1958) 3477.
[58] G.W. Watson, E.T. Kelsey, N.H. de Leeuw, D.J. Harris, S.C. Parker, J. Chem. Soc., Faraday Trans. 92 (1996) 433.
[59] S. Fleming, A.L. Rohl, Z. Krist. 220 (2005) 580.
[60] K. Fujino, S. Sasaki, Y. Takeuchi, R. Sadanaga, Acta. Cryst. B 37 (1981) 513.
[61] K. Iishi, Am. Mineral. 63 (1978) 1198.
[62] A.L. Rohl, K. Wright, J.D. Gale, Am. Mineral. 88 (2003) 921.
[63] A. Banerjee, N. Adams, J. Aimons, R. Shepard, J. Phys. Chem. 89 (1985) 52.
[64] K. Modig, B.G. Pfrommer, B. Halle, Phys. Rev. Lett. 90 (2003) 075502.
[65] B. Kamb, Water and aqueous solutions, in: R.A. Horne (Ed.), Wiley, New York, 1972.
[66] B. Fubini, V. Bolis, M. Bailes, F.S. Stone, Solid St. Ionics 32/33 (1989) 258.
[67] A. Stirling, M. Bernasconi, M. Parinello, J. Chem. Phys. 118 (2003) 8917.
[68] E.A. Leed, C.G. Pantano, J. Non-Cryst. Solids 325 (2003) 48.